Long-Distance Distribution of Atom-Photon Entanglement at Telecom Wavelength

Tim van Leent,[1,2,‡] Matthias Bock,[3,‡] Robert Garthoff,[1,2,‡] Kai Redeker,[1,2] Wei Zhang,[1,2] Tobias Bauer,[3] Wenjamin Rosenfeld,[1,2,4] Christoph Becher,[3,*] and Harald Weinfurter[1,2,4,†]

[1]*Fakultät für Physik, Ludwig-Maximilians-Universität München, Schellingstraße 4, 80799 München, Germany*
[2]*Munich Center for Quantum Science and Technology (MCQST), Schellingstraße 4, 80799 München, Germany*
[3]*Fachrichtung Physik, Universität des Saarlandes, Campus E2.6, 66123 Saarbrücken, Germany*
[4]*Max-Planck Institut für Quantenoptik, Hans-Kopfermann-Straße 1, 85748 Garching, Germany*

(Received 30 August 2019; published 10 January 2020)

Entanglement between stationary quantum memories and photonic channels is the essential resource for future quantum networks. Together with entanglement distillation, it will enable efficient distribution of quantum states. We report on the generation and observation of entanglement between a ^{87}Rb atom and a photon at telecom wavelength transmitted through up to 20 km of optical fiber. For this purpose, we use polarization-preserving quantum frequency conversion to transform the wavelength of a photon entangled with the atomic spin state from 780 nm to the telecom S band at 1522 nm. We achieve an unprecedented external device conversion efficiency of 57% and observe an entanglement fidelity between the atom and telecom photon of $\geq 78.5 \pm 0.9\%$ after transmission through 20 km of optical fiber, mainly limited by decoherence of the atomic state. This result is an important milestone on the road to distribute quantum information on a large scale.

DOI: 10.1103/PhysRevLett.124.010510

Introduction.—Quantum repeaters will allow for scalable quantum networks [1,2], which are essential for large-scale quantum communication and distributed quantum computing. In such networks, photon mediated entanglement is distributed among quantum memories at stationary nodes. Various candidates exist to serve as quantum memory, which also provide the light-matter interface in these nodes, for example, trapped neutral atoms [3,4], atomic ensembles [5–7], trapped ions [8,9], nitrogen-vacancy (NV) centers [10,11], quantum dots [12,13], or rare earth ions in solids [14,15].

For single atoms, several critical capabilities required to serve as a network node have recently been demonstrated. This concerns, in particular, atom-atom quantum logic gates [16–18], long qubit storage times [19], high-fidelity heralded entanglement over hundreds of meters [20,21], and scalability of the number of individually addressable trapped atoms [22–24]. These achievements make single trapped atoms a promising candidate to develop a first quantum repeater link.

A capability not demonstrated for single atoms so far, however, is the distribution of entanglement at telecom wavelengths, which is indispensable for long, fiber-based quantum network links. By employing quantum frequency conversion (QFC) to the telecom wavelength [25–28], the attenuation in fibers can be minimized while enabling the use of existing telecommunication infrastructure to economically realize network links. Recently, such concepts have been used to demonstrate entanglement between a telecom photon and an atomic ensemble [29–32], a trapped ion [33,34], or a NV center [35].

Here we report on the generation and detection of entanglement between a ^{87}Rb atom and a photon at the telecom wavelength over long fiber links. The scheme starts with entangling the atomic spin state with the polarization state of a spontaneously emitted photon [3]. Subsequently, the wavelength of the photon is converted to the telecom S band while preserving its polarization state and transferred over several kilometers of optical fiber [33]. The entanglement is analyzed by measuring atom-photon state correlations in two bases. Based on our results, we analyze the applicability of this scheme for long-distance quantum links.

Methods.—The experimental setup consists of a single atom trap with high-NA optics to collect the atomic fluorescence, a polarization-preserving quantum frequency converter in Sagnac configuration, and a polarization analyzer which is connected via single mode fibers of different lengths. For details, see Fig. 1.

The experimental sequence starts by storing a single ^{87}Rb atom in an optical dipole trap [3,20] and preparing it in the initial state $5^2S_{1/2}\ |F = 1, m_F = 0\rangle$ via optical pumping. Next, a short laser pulse (22 ns FWHM) excites the atom to the state $5^2P_{3/2}\ |F' = 0, m_{F'} = 0\rangle$ (Fig. 1). In the subsequent spontaneous decay, the atomic spin state becomes entangled with the polarization state of the photon emitted along the quantization (z) axis. This results in the following maximally entangled atom-photon state

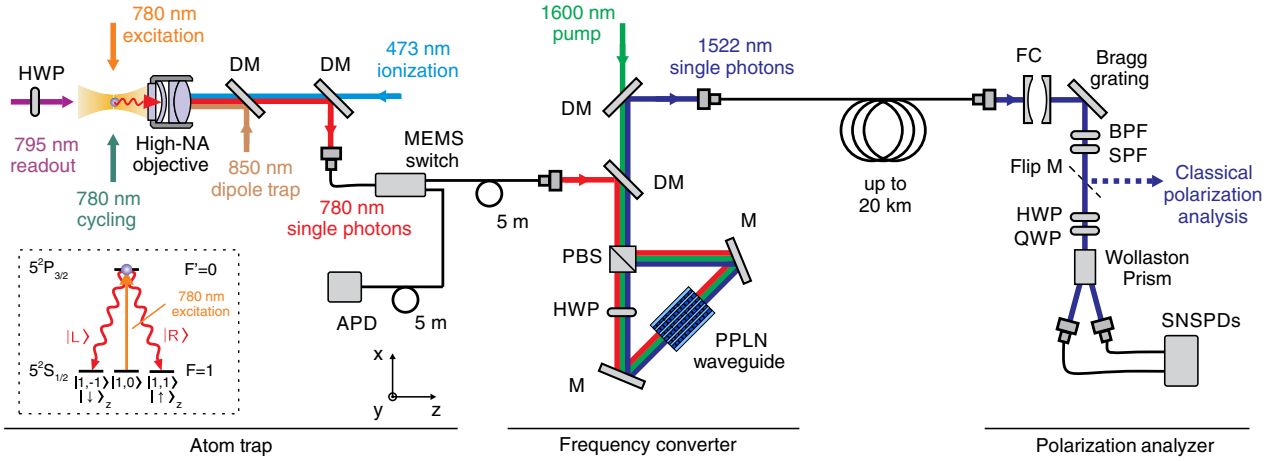

FIG. 1. Experimental setup and entanglement generation scheme. A single ^{87}Rb atom (upper left side), serving as quantum memory, is stored in the focus of a dipole trap (850 nm wavelength, 2.05 μm waist, and 42 mW power), where a high-NA objective collects the atomic fluorescence. The atom-photon entanglement is generated in the spontaneous decay following the excitation to the state $5^2P_{3/2}$ $|F' = 0, m_{F'} = 0\rangle$. The MEMS switch guides the emitted photons toward the frequency converter where the 780 nm single photons are overlapped with 1600 nm pump light within a PPLN waveguide in a Sagnac-type interferometer to transfer the entanglement to 1522 nm photons. In the polarization analyzer, the single photons are first spectrally filtered by a Fabry-Perot filter cavity (FC), volume Bragg grating, bandpass filter (BPF), and short-pass filter (SPF). Next, after setting the analysis basis with a half-wave plate (HWP) and a quarter-wave plate (QWP) and splitting the polarization components by a Wollaston prism, the single photons are detected with two SNSPDs. Classical reference light, inserted along the readout path, can be coupled out with a flip mirror to analyze and compensate for polarization drifts. Further abbreviations used are mirror (M) and dichroic mirror (DM).

$$|\Psi\rangle_{\text{atom-photon}} = \frac{1}{\sqrt{2}}(|\downarrow\rangle_z|L\rangle + |\uparrow\rangle_z|R\rangle) = \frac{1}{\sqrt{2}}(|\downarrow\rangle_x|V\rangle + |\uparrow\rangle_x|H\rangle), \quad (1)$$

where $|L\rangle$ and $|R\rangle$ denote left- and right-circular photonic polarization states, $|H\rangle$ and $|V\rangle$ denote the horizontal and vertical linear photonic polarization states, and $|\downarrow\rangle$ and $|\uparrow\rangle$ denote the atomic qubit state which, e.g., for the quantization axis z, corresponds to the states $|F = 1, m_F = -1\rangle$ or $|F = 1, m_F = +1\rangle$, respectively.

A microelectromechanical systems (MEMS) switch is used to either guide the atomic fluorescence to a silicon avalanche photodiode (APD) during loading the trap or to the frequency converter during the state preparation and excitation cycles. These cycles are repeated until a single telecom photon is detected at the polarization analyzer, whereby the atom is cooled for 350 μs after each 40 excitations in order to minimize the thermal motion in the trap. The excitation rate is limited mainly by the travel time of the photon through the optical fiber, resulting in an average excitation rate of 7.3 kHz for the 20 km fiber.

To obtain the necessary performance for the presented experiment, the coherence time of the atomic state is prolonged to hundreds of microseconds by suppressing small ($\sim$ milligauss) magnetic field fluctuations with a 42 mG constant magnetic field along the y axis. Currently, the dominant decoherence effect is position-dependent dephasing caused by longitudinal field components of the strongly focused dipole trap [36,37]. On the efficiency side, by implementing a custom designed high-NA objective, an overall efficiency of about 7.5×10^{-3} is achieved without conversion for detecting a photon with the APD ($\sim$55% efficiency) after an excitation attempt.

The polarization-preserving QFC to the telecom S band at 1522 nm is realized by difference-frequency generation in a periodically poled lithium niobate (PPLN) waveguide. To this end, the single photons at 780 nm are mixed with a strong cw pump field at 1600 nm within a waveguide in a Sagnac-type setup [31]. The input polarization is split into two arms with a polarizing beam splitter (PBS), whereby a half-wave plate (HWP) is introduced in one of the arms such that the two counterpropagating beams have the same polarization when entering the waveguide. The conversion efficiency of both arms is set equal by fine-tuning the pump field powers; see Fig. 2.

Various spectral filtering stages efficiently separate the single telecom photon from the strong pump field and the noise induced by the pump field via anti-Stokes Raman scattering in the waveguide. For this purpose, we introduce a combination of two short-pass filters (SPFs) with a cutoff at 1560 nm, a bandpass filter (BPF) at 1535 nm with a bandwidth of 30 nm FWHM, a volume Bragg grating (25 GHz FWHM), and a Fabry-Perot filter cavity (FC) with a finesse of 700 and a bandwidth of 27 MHz FWHM. The latter is locked to the pump laser at 1600 nm while having a further resonance at the telecom single-photon frequency. See Sec. I of the Supplemental Material [39] for more details about the QFC.

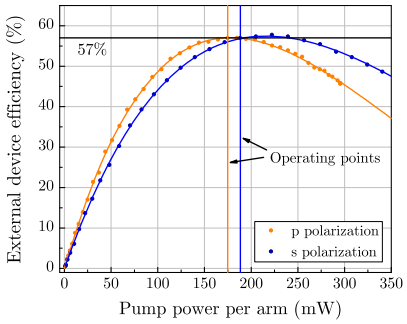

FIG. 2. External device efficiency of the frequency converter. The external device efficiency (η) of the two polarization components depends on the pump power (P) in the respective arm. The data are fitted with $\eta(P) = \eta_{\max} \sin^2(\sqrt{\eta_{\mathrm{nor}} P} L)$ [38]. The power in each arm is set to the operating point such that both conversion efficiencies are equal and one efficiency is maximized, 175 and 189 mW for the p- and s-polarization arms, respectively. At this point, the external device efficiency equals 57%.

The external device efficiency of the frequency converter, defined from the input fiber of the converter until the first wave plate of the polarization analyzer and including a 50 m optical fiber, equals 57%. This is, to the best of our knowledge, the highest external device efficiency reported so far. The efficiency is limited by the transmission through optical elements (82.6%), fiber coupling (87.8%), waveguide coupling (90.0%), and spectral filtering (90.7%), which reduce the high internal conversion efficiency of 96.2%.

The polarization state of the telecom photons is analyzed after propagating through up to 20 km of optical fiber (Corning SMF-28). Single photons are detected by two superconducting nanowire single-photon detectors (SNSPDs) with efficiencies of 16% and 18% at 1522 nm. Detection events are accepted within a hardwired interval of 50 ns, which results in accepting approximately 2/3 of the converted single photons. Polarization rotations in the complete single-photon beam path are analyzed and can be compensated for by using classical reference light and a fiber polarization controller [21].

Following a successful photon detection event, the atomic spin state is analyzed using a state-selective ionization scheme. The state selectivity is controlled by the polarization of the readout pulse; see Sec. II of the Supplemental Material [39] for more details.

Results.—We analyzed the entanglement between the atom and photon at the telecom wavelength after a 20 km (A), 10 km (B), and 50 m (C) optical fiber. Furthermore, to investigate possible noise induced by the QFC, a reference measurement was performed without frequency conversion (D). For measurements C and D, we applied an atomic state detection delay of 51 μs to make the loss in fidelity due to atomic state decoherence comparable to measurement B. All results are summarized in Table I.

TABLE I. Observation of atom-photon entanglement for different experimental configurations. The measurement configurations A, B, C, and D differ in optical fiber length, detection wavelength, and/or atomic state detection delay. The fidelity is obtained via Eq. (2), where the visibilities are fitted from the measured correlation probabilities. The S parameter (CHSH) is calculated directly from the measured Bell states.

	(A)	(B)	(C)	(D)
Fiber length	20 km	10 km	50 m	5 m
Wavelength	1522 nm	1522 nm	1522 nm	780 nm
Readout delay	102 μs	51 μs	51 μs	51 μs
Fidelity (%)	78.5 ± 0.9	84.3 ± 0.9	88.0 ± 0.8	89.7 ± 0.7
S (CHSH)	2.12 ± 0.05	2.37 ± 0.04	2.41 ± 0.03	2.49 ± 0.03
SNR	25.1	23.2	32.3	934.2

A photon detection time histogram and corresponding atom-photon state correlations over 20 km of optical fiber are shown in Figs. 3(a) and 3(b), respectively. In this measurement, 11 335 events were observed within 360 min with an overall efficiency of detecting a telecom photon after an excitation attempt of 0.173×10^{-3}. When optimizing the experiment for efficiency, e.g., by employing efficient single-photon detectors (> 85%) and replacing the lossy MEMS switch (25% loss), we expect an improvement of the overall efficiency by about 1 order of magnitude. The event rate in all measurements is ~35/min, mainly limited by the atom loading time of about 1 s since the atom is lost during the state readout process in approximately half of the cases.

The signal-to-noise ratio (SNR) of the photon detection is limited mainly by the QFC pump laser induced noise and detector dark counts; see Sec. I of the Supplemental Material [39] for details. For measurement A, these contributions amounted to 128 and 18 cps summed over both detectors, respectively. The SNR of 25.1 corresponds to our expectation, taking into account the 50 ns photon acceptance interval and the overall efficiency mentioned above. Variations in the SNR between measurements A, B, and C originate from different fiber lengths as well as from slight laser power fluctuations in the atomic state preparation and excitation cycles.

To analyze the entanglement, the photonic polarization was measured in the H/V (horizontal/vertical) and D/A (diagonal/antidiagonal) basis, while varying the atomic analysis angle (i.e., readout polarization). The visibilities of the measured states are obtained by fitting the data with sinusoidal curves. The average visibility ($\bar{V}$) of the entangled state is estimated by assuming that the visibility in the third (unmeasured) basis is equal to the D/A basis. This results in estimated average visibilities of $74.2 \pm 1.0\%$, $81.2 \pm 1.1\%$, $85.6 \pm 0.9\%$, and $87.4 \pm 0.6\%$ for measurements A, B, C, and D, respectively. Note that the visibility of the detected photon state $|V\rangle$ [e.g., the red

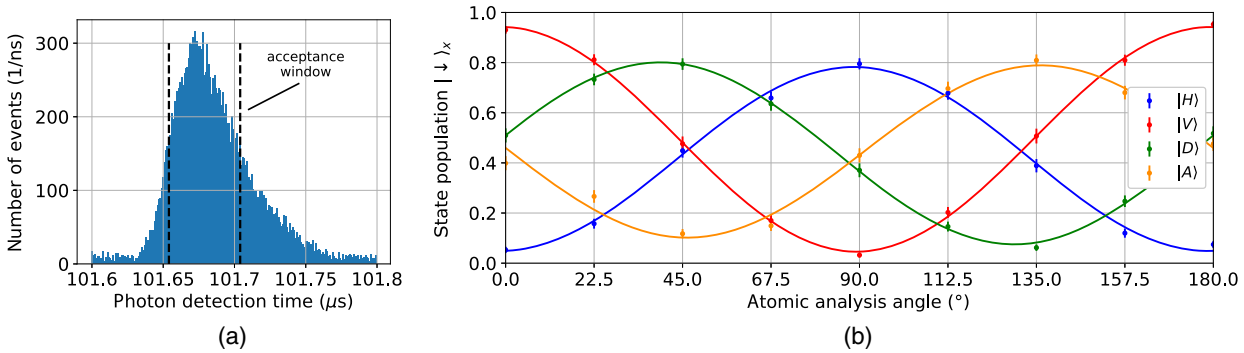

FIG. 3. Observation of atom-photon entanglement over 20 km of optical fiber (A). (a) Detection time histogram of the frequency converted photons. Within a hardwired acceptance window of 50 ns, indicated with dashed lines, approximately $2/3$ of the converted single photons were accepted. Note that the QFC does not influence the photon shape [25]; see Ref. [20] for an unconverted photon shape. (b) The corresponding atom-photon state correlations in two bases (H/V and D/A) for varying atomic analysis angles (i.e., readout polarization, where 0° corresponds to vertical polarization). The sinusoidal fits give estimated visibilities of $73.4 \pm 2.0\%$, $89.6 \pm 1.1\%$, $72.5 \pm 1.1\%$, and $68.6 \pm 4.1\%$ for horizontal $|H\rangle$, vertical $|V\rangle$, diagonal $|D\rangle$, and antidiagonal $|A\rangle$ photonic linear polarization states, respectively. This results in an estimated state fidelity of $\geq 78.5 \pm 0.9\%$.

curve in Fig. 3(b)] is significantly higher than the other states since the resulting atomic state is insensitive to the position-dependent dephasing of the atomic state, which is the dominant decoherence effect for all other states.

To compute a fidelity based on the measured visibilities, one needs to consider that the atom is a spin-1 system. Hence, also a third atomic spin state can be populated ($5^2S_{1/2}$ $|F = 1, m_F = 0\rangle$). Imperfections in the experiment, such as small magnetic fields ($\sim$ milligauss) in a direction not coinciding with the quantization axis, can lead to a population in this state. Accordingly, assuming isotropic dephasing toward white noise in the 2×3 state space, a lower bound on the fidelity of the entangled state is given by

$$F \geq \frac{1}{6} + \frac{5}{6}\bar{V}, \tag{2}$$

which results in fidelities of $\geq 78.5 \pm 0.9\%$, $84.3 \pm 0.9\%$, $88.0 \pm 0.8\%$, and $89.7 \pm 0.7\%$ relative to maximally entangled states for measurements A, B, C, and D, respectively. For measurement A, contributions to the loss in fidelity are the imperfect atomic state readout (3%), atomic state decoherence (11%), SNR in the photon detection (4%), and experimental drifts (3%).

The influence of the QFC on the state fidelity is best analyzed by comparing measurement C ($88.0 \pm 0.8\%$) and D ($89.5 \pm 0.5\%$) since the experimental configurations are most similar. For these measurements, the difference in fidelity can be explained solely by their difference in SNR (3%).

When comparing measurement B ($84.3 \pm 0.9\%$) and C ($88.0 \pm 0.8\%$), the difference in fidelity is more than what can be expected from the lower SNR alone (1%). We attribute the additional fidelity loss (3%) in measurement B to instabilities in the experiment, such as fiber polarization, magnetic field, and laser power drifts. The difference in fidelity between measurements A ($78.5 \pm 0.9\%$) and B ($84.3 \pm 0.9\%$) originates primarily from atomic state decoherence (5%).

All four measurements also include two setting combinations for a Clauser-Horne-Shimony-Holt (CHSH)-Bell test [47]. The CHSH inequality requires two measurement settings for the photonic state (H/V and D/A) and two measurement settings for the atomic state (22.5° or 157.5° and 67.5° or 112.5°). The resulting S parameters, all clearly violating the CHSH-Bell inequality, are listed in Table I.

Outlook.—The next milestone toward large-scale quantum networks is to distribute heralded entanglement at the telecom wavelength between two distant atomic memories via the entanglement swapping protocol [20]. For this purpose, it is necessary to introduce frequency conversion for a second atom trap and install a set of SNSPDs optimized for 1522 nm.

The expected atom-atom entanglement fidelity for varying distance is estimated by $F_{a\text{-}a} \geq 1/9 + 8/9\bar{V}$, where the average atom-atom visibility $\bar{V}$ is estimated by squaring the corresponding atom-photon visibility and taking into account a 94% two-photon interference contrast [20]. Furthermore, we assume that the measurement needed for the entanglement swapping is performed at a middle station such that the atomic coherence time needed to distribute atom-photon and atom-atom entanglement over the same distance evens up.

Figure 4 shows the expected entanglement fidelities for a range of distances between the quantum memories. Below 1 km, the performance is limited by imperfections in the atomic state preparation and analysis. For longer distances, the atomic state decoherence due to the position-dependent dephasing will significantly reduce the fidelity [37]. A new

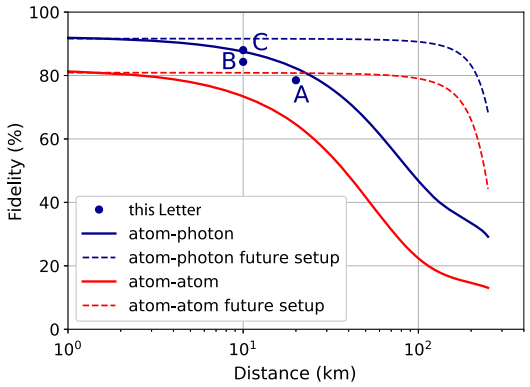

FIG. 4. Expected atom-photon and atom-atom entanglement fidelities. Points marked *A*, *B*, and *C* correspond to the measurements presented in the text and summarized in Table I. The expected fidelity for short distances (< 1 km) is mainly limited by the imperfect atomic state preparation and readout. For distances < 100 km, the fidelity is also reduced by atomic state decoherence due to position-dependent dephasing, which could be strongly suppressed in a future setup. For distances > 100 km, detector dark counts will eventually limit the fidelity.

trap geometry, involving a standing wave dipole trap, promises to strongly reduce this decoherence effect. The expected fidelities for this future setup are for large distances eventually limited by detector dark counts.

Using the current trap geometry, we expect an atom-atom entanglement fidelity of 65% over 20 km with an event rate of $1/$ min. By improving the trap geometry, we expect this fidelity to increase to 81%. Together with entanglement distillation [11], this allows for an efficient distribution of quantum states over long distances.

Conclusion.—Thanks to the record high external device efficiency of 57% for the polarization-preserving QFC and improved collection optics for the atomic fluorescence, atom-photon entanglement was distributed and observed at a high rate with a fidelity of at least $78.5 \pm 0.9\%$ over 20 km optical fiber. Implementing realistic improvements and extrapolating to even longer distances shows that entanglement distribution between atomic memories is feasible with a fidelity of more than 80% over up to 100 km, thereby forming a valuable component for future quantum-repeater-based quantum networks.

We thank Benjamin Kambs and Stephan Kucera for the valuable discussions regarding the QFC, Harald Giessen for lending us the 10 km fiber, and Matthias Kreis for the technical support on the cavity locking electronics. We acknowledge funding by the German Federal Ministry of Education and Research (Bundesministerium für Bildung und Forschung, BMBF) within the projects Q.com.Q and Q.Link.X (Contracts No. 16KIS0127, No. 16KIS0123, No. 16KIS0864, and No. 16KIS0880) and by the Deutsche Forschungsgemeinschaft (German Research Foundation, DFG) under Germany's Excellence Strategy, Project No. EXC-2111-390814868.

*christoph.becher@physik.uni-saarland.de
†h.w@lmu.de
‡These authors contributed equally to this work.

[1] H.-J. Briegel, W. Dür, J. I. Cirac, and P. Zoller, Phys. Rev. Lett. **81**, 5932 (1998).
[2] H. J. Kimble, Nature (London) **453**, 1023 (2008).
[3] J. Volz, M. Weber, D. Schlenk, W. Rosenfeld, J. Vrana, K. Saucke, C. Kurtsiefer, and H. Weinfurter, Phys. Rev. Lett. **96**, 030404 (2006).
[4] S. Ritter, C. Nölleke, C. Hahn, A. Reiserer, A. Neuzner, M. Uphoff, M. Mücke, E. Figueroa, J. Bochmann, and G. Rempe, Nature (London) **484**, 195 (2012).
[5] M. D. Lukin, S. F. Yelin, and M. Fleischhauer, Phys. Rev. Lett. **84**, 4232 (2000).
[6] A. Kuzmich, W. Bowen, A. Boozer, A. Boca, C. Chou, L.-M. Duan, and H. Kimble, Nature (London) **423**, 731 (2003).
[7] N. Sangouard, C. Simon, H. de Riedmatten, and N. Gisin, Rev. Mod. Phys. **83**, 33 (2011).
[8] B. Blinov, D. Moehring, L.-M. Duan, and C. Monroe, Nature (London) **428**, 153 (2004).
[9] L.-M. Duan and C. Monroe, Rev. Mod. Phys. **82**, 1209 (2010).
[10] C. Kurtsiefer, S. Mayer, P. Zarda, and H. Weinfurter, Phys. Rev. Lett. **85**, 290 (2000).
[11] N. Kalb, A. A. Reiserer, P. C. Humphreys, J. J. Bakermans, S. J. Kamerling, N. H. Nickerson, S. C. Benjamin, D. J. Twitchen, M. Markham, and R. Hanson, Science **356**, 928 (2017).
[12] C. Santori, D. Fattal, J. Vučković, G. S. Solomon, and Y. Yamamoto, Nature (London) **419**, 594 (2002).
[13] L. I. Childress, J. M. Taylor, A. Sørensen, and M. D. Lukin, Phys. Rev. A **72**, 052330 (2005).
[14] K. Kutluer, M. Mazzera, and H. de Riedmatten, Phys. Rev. Lett. **118**, 210502 (2017).
[15] C. Laplane, P. Jobez, J. Etesse, N. Gisin, and M. Afzelius, Phys. Rev. Lett. **118**, 210501 (2017).
[16] S. Welte, B. Hacker, S. Daiss, S. Ritter, and G. Rempe, Phys. Rev. X **8**, 011018 (2018).
[17] M. Saffman, T. G. Walker, and K. Mølmer, Rev. Mod. Phys. **82**, 2313 (2010).
[18] T. Wilk, A. Gaëtan, C. Evellin, J. Wolters, Y. Miroshnychenko, P. Grangier, and A. Browaeys, Phys. Rev. Lett. **104**, 010502 (2010).
[19] M. Körber, O. Morin, S. Langenfeld, A. Neuzner, S. Ritter, and G. Rempe, Nat. Photonics **12**, 18 (2018).
[20] J. Hofmann, M. Krug, N. Ortegel, L. Gérard, M. Weber, W. Rosenfeld, and H. Weinfurter, Science **337**, 72 (2012).
[21] W. Rosenfeld, D. Burchardt, R. Garthoff, K. Redeker, N. Ortegel, M. Rau, and H. Weinfurter, Phys. Rev. Lett. **119**, 010402 (2017).
[22] M. Endres, H. Bernien, A. Keesling, H. Levine, E. R. Anschuetz, A. Krajenbrink, C. Senko, V. Vuletic, M. Greiner, and M. D. Lukin, Science **354**, 1024 (2016).
[23] D. Barredo, S. De Léséleuc, V. Lienhard, T. Lahaye, and A. Browaeys, Science **354**, 1021 (2016).
[24] D. Ohl de Mello, D. Schäffner, J. Werkmann, T. Preuschoff, L. Kohfahl, M. Schlosser, and G. Birkl, Phys. Rev. Lett. **122**, 203601 (2019).

[25] S. Zaske, A. Lenhard, C. A. Keßler, J. Kettler, C. Hepp, C. Arend, R. Albrecht, W.-M. Schulz, M. Jetter, P. Michler *et al.*, Phys. Rev. Lett. **109**, 147404 (2012).
[26] S. Ates, I. Agha, A. Gulinatti, I. Rech, M. T. Rakher, A. Badolato, and K. Srinivasan, Phys. Rev. Lett. **109**, 147405 (2012).
[27] K. De Greve, L. Yu, P. L. McMahon, J. S. Pelc, C. M. Natarajan, N. Y. Kim, E. Abe, S. Maier, C. Schneider, M. Kamp *et al.*, Nature (London) **491**, 421 (2012).
[28] R. Ikuta, Y. Kusaka, T. Kitano, H. Kato, T. Yamamoto, M. Koashi, and N. Imoto, Nat. Commun. **2**, 537 (2011).
[29] Y. O. Dudin, A. G. Radnaev, R. Zhao, J. Z. Blumoff, T. A. B. Kennedy, and A. Kuzmich, Phys. Rev. Lett. **105**, 260502 (2010).
[30] B. Albrecht, P. Farrera, X. Fernandez-Gonzalvo, M. Cristiani, and H. de Riedmatten, Nat. Commun. **5**, 3376 (2014).
[31] R. Ikuta, T. Kobayashi, T. Kawakami, S. Miki, M. Yabuno, T. Yamashita, H. Terai, M. Koashi, T. Mukai, T. Yamamoto *et al.*, Nat. Commun. **9**, 1997 (2018).
[32] Y. Yu, F. Ma, X.-Y. Luo, B. Jing, P.-F. Sun, R.-Z. Fang, C.-W. Yang, H. Liu, M.-Y. Zheng, X.-P. Xie *et al.*, arXiv:1903.11284.
[33] M. Bock, P. Eich, S. Kucera, M. Kreis, A. Lenhard, C. Becher, and J. Eschner, Nat. Commun. **9**, 1998 (2018).
[34] V. Krutyanskiy, M. Meraner, J. Schupp, V. Krcmarsky, H. Hainzer, and B. Lanyon, npj Quantum Inf. **5**, 72 (2019).
[35] A. Tchebotareva, S. L. N. Hermans, P. C. Humphreys, D. Voigt, P. J. Harmsma, L. K. Cheng, A. L. Verlaan, N. Dijkhuizen, W. de Jong, A. Dréau, and R. Hanson, Phys. Rev. Lett. **123**, 063601 (2019).
[36] R. Garthoff, T. van Leent, K. Redeker, W. Zhang, W. Rosenfeld, and H. Weinfurter (to be published).
[37] D. Burchardt, Ph.D. thesis, Ludwig-Maximilians-Universität München, 2017.
[38] S. Zaske, A. Lenhard, and C. Becher, Opt. Express **19**, 12825 (2011).
[39] See Supplemental Material at http://link.aps.org/supplemental/10.1103/PhysRevLett.124.010510, which includes Refs. [40–46], for further details about the quantum frequency converter and atomic state readout.
[40] F. Rohde, M. Almendros, C. Schuck, J. Huwer, M. Hennrich, and J. Eschner, J. Phys. B **43**, 115401 (2010).
[41] V. Krutyanskiy, M. Meraner, J. Schupp, and B. P. Lanyon, Appl. Phys. B **123**, 228 (2017).
[42] S. Ramelow, A. Fedrizzi, A. Poppe, N. K. Langford, and A. Zeilinger, Phys. Rev. A **85**, 013845 (2012).
[43] F. Kaiser, P. Vergyris, A. Martin, D. Aktas, M. P. De Micheli, O. Alibart, and S. Tanzilli, Opt. Express **27**, 25603 (2019).
[44] M. A. Albota, F. N. Wong, and J. H. Shapiro, J. Opt. Soc. Am. B **23**, 918 (2006).
[45] N. Maring, D. Lago-Rivera, A. Lenhard, G. Heinze, and H. de Riedmatten, Optica **5**, 507 (2018).
[46] N. Ortegel, Ph.D. thesis, Ludwig-Maximilians-Universität München, 2016.
[47] J. F. Clauser, M. A. Horne, A. Shimony, and R. A. Holt, Phys. Rev. Lett. **23**, 880 (1969).